Graphite-SiOx Electrodes with a Biopolymeric Binder for Li-Ion Batteries: Predicting the Cycle Life Performance from Physical Properties

Drakopoulos, Stavros X.; Cowell, Thomas; Kendrick, Emma

DOI:
10.1021/acsaem.3c00488

Document Version
Publisher's PDF, also known as Version of record

ACS APPLIED ENERGY MATERIALS

www.acsaem.org Article

Graphite-SiO_x Electrodes with a Biopolymeric Binder for Li-Ion Batteries: Predicting the Cycle Life Performance from Physical Properties

Stavros X. Drakopoulos, Thomas Cowell, and Emma Kendrick*

Cite This: https://doi.org/10.1021/acsaem.3c00488 Read Online

ACCESS | Metrics & More | Article Recommendations | Supporting Information

ABSTRACT: Low-environmental-impact binder systems are required for lithium-ion battery electrodes that exhibit good cohesive and adhesive strengths, flexibility, optimized microstructures for ions, and electronic conductivities. In this work, carrageenan gum is employed as a green binder system for graphite-SiO_x anodes of various physical characteristics (porosity and active mass). A simple current interrupt test is used to elucidate the contributing ohmic and charge transfer resistances, showing increase in both, related to the mass loading, porosity, and state of charge. The contribution of SiO_x to the reversible capacity was observed to fade in the first 20−30 cycles. To describe the cycle life, an empirical model that directly relates the porosity and mass loading to the cycle life is presented. A relationship between the physical and electrochemical properties has been explored to achieve maximum cycle life. This method may enable faster screening of electrode formulations and prediction of cycle life of this and other electrode types.

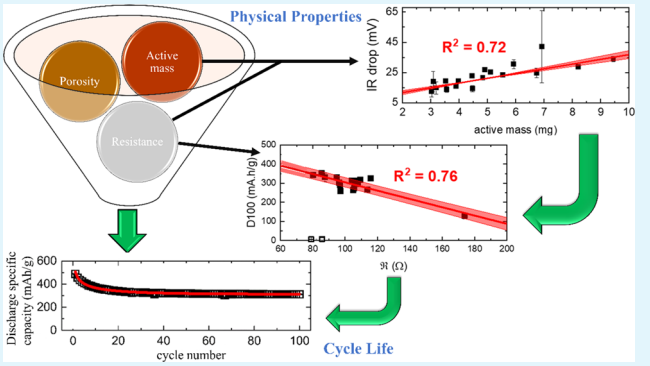

KEYWORDS: *lithium-ion batteries, graphite, silicon suboxide, electrode manufacturing, carrageenan binder*

1. INTRODUCTION

The rechargeable Li-ion battery is a fundamental necessity in modern society, being used in devices including cell phones, laptop computers, and digital cameras.[1] Decades of incremental improvements have made today's rechargeable batteries safer, with longer life and higher densities that are now being used in electric vehicles.[2−4] With this broad applicability of Li-ion batteries, it is important to take into account the environmental impact that they have and design the manufacturing, materials, processing, and recycling with this in mind.[5−9]

The most common anode material for Li-ion batteries is graphite, despite its relatively low specific capacity (372 mA·h/g), because of its cycle life stability attributed to its low volume expansion during lithiation and delithiation.[10−13] In order to improve the capacity performance, but not compromise on the volume expansion, silicon suboxide (SiO_x; 1965 mA·h/g) can be mixed with graphite at low amounts to boost the specific capacity that is attractive for high-energy requirements.[14] SiO_x is less conductive than graphite (6.7×10^{-4} S cm^{-1} compared to $\sim 10^4$ S cm^{-1}) and thus a conductive 3D network with carbon black, or alternative conductive additives, is used to increase the electrically conductive pathways and enable the electron transfer from the surface of the electrode to the current collector.[15−17] In addition, the presence of the polymeric binder also increases the resistivity of the coatings despite its importance toward the mechanical stability of the electrode, and thus its presence is preferred at a minimum.[18] Its role is to bind the active materials and conductive additive to the current collector and affect the electrode-current collector adhesion properties.[19,20] In order to reduce cost and improve the environmental impact of Li-ion battery electrodes, water-soluble binders can be utilized, most commonly carboxyl methylcellulose (CMC) and styrene-butadiene rubber (SBR).[8,21−23] The ideal binder should allow the volume expansion of the active mass during lithiation/delithiation cycles and augment the pulverization of the electrode and thus the failure of the battery after many charge/discharge cycles.[24] Other polymeric natural or bioinspired binders like carrageenan have been introduced and electrochemically investigated in the literature in the past decade.[25−28] Among other similar water-based binders, carrageenan has the potential to replace the commonly used oil-based SBR, thus simplifying the electrode manufacturing in

Received: February 24, 2023
Accepted: May 3, 2023

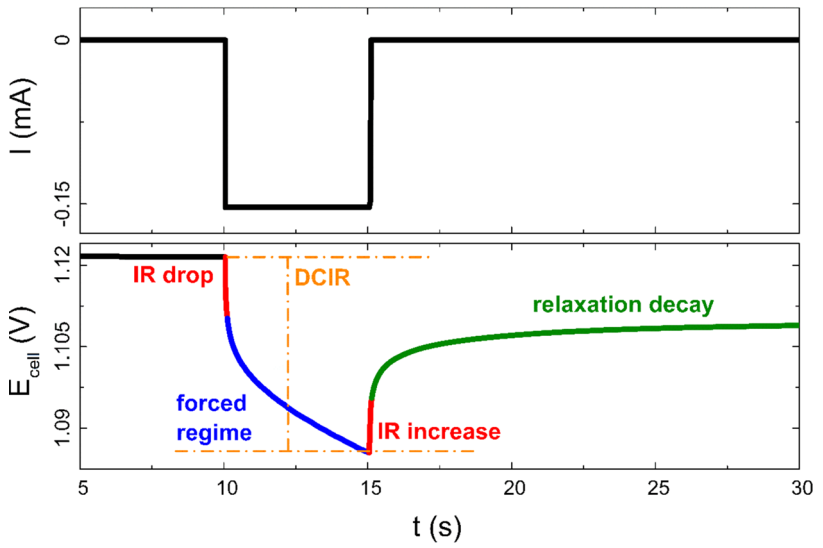

Figure 1. Voltage response during a discharge DCIR pulse at 99% SoC.

a more environmentally friendly way, without compromising the mechanical flexibility required.[23] Compared to commercially standard polymeric binders like CMC and PVDF, battery cells with carrageenan exhibit superior specific capacity, more stable cycle life performance, and improved conductivity values.[29−31]

The microstructure of the electrodes is heavily influenced by the manufacturing process (mixing, coating, drying, and calendering) and consequently affects the resulting battery performance and cost.[32,33] By applying mechanical compression through twin-roll calendering, the porosity can be tuned in order to achieve the optimum combination of electronic and ionic conductivities by altering the pore size and conductive network.[34−36]

The energy efficiency and lost heat during the operation and cycle life of a battery are heavily governed by the internal resistance of the cell and therefore, understanding its precise value is paramount to effectively design batteries for specific applications.[37,38] In order to obtain this information, the direct current internal resistant (DCIR) or intermittent current interruption (ICI) method can be applied.[39] The DCIR method provides a simple way to discern the individual contributions on cell impedance (series, charge transfer, and diffusion resistance) and can be implemented under different conditions (temperature, pulse duration/magnitude, and state of charge).[40,41] By reducing the pulse duration down to several milliseconds, the diffusion resistance attributed to mass transfer is considered negligible and can be omitted, and therefore the ohmic resistance and reaction overpotential (charge transfer resistance) only are probed.[42] Since there is a correlation between resistance increase, capacity diminish, and battery deterioration, DCIR is also an important piece of information regarding cycle life performance.[43] The information extracted from the DCIR method can be compared with that obtained from electrochemical impedance spectroscopy (EIS).[44] The voltage characteristics during and after a current pulse are described in Figure 1 and in the literature.[38] The voltage relaxation (relaxation decay) is due to the gradient of lithium ions that minimizes the energy state during lithiation or delithiation. This relaxation process is affected by the concentration of lithium ions and is characterized by the relaxation time.[45]

In the present work, the effects of coat weight and porosity upon graphite-SiO_x electrodes employing carrageenan as binder were investigated and the physical parameters mapped against the electrochemical properties. Carrageenan was chosen due to its promising electrochemical and cycle life properties, as reported in the literature and mentioned earlier in the text. The effects of active mass and porosity on DCIR values right after formation are discussed. The aim is to find the relationships of parameters that can be determined accurately at an early stage of electrode manufacturing or cell testing (active mass, porosity, open-circuit voltage, first cycle loss, IR drop) with the resulting cycle life performance after 100 cycles (discharge specific capacity) for early screening. A new empirical model based on the physical parameters that can describe the discharge specific capacity in the present dataset is proposed.

2. EXPERIMENTAL PROCEDURES

2.1. Electrode Formulation and Manufacturing. The graphite-SiO_x electrode composition included graphite 76.5% w/w and SiO_x (BTR) 13.5% as the active materials in an 85:15 ratio, carbon black (C45, Timcal) conductive carbon at 5% w/w, and iota-carrageenan (Fisher) at 5% w/w. The materials were added to a 150 mL mixing vessel and subsequently 1.25 g of carrageenan gum with 10 g of water was mixed in an ARE-250 Thinky Mixer for 3 min at 1300 rpm. Then, 1.25 g of C45 with 8.75 g of water was added, with the sample was mixed again for 3 min at 1300 rpm. Finally, 19.125 g of graphite and 3.375 g of SiO_x with an additional 18.75 g of water were added and mixed using the same parameters to produce an ink.

After mixing, the slurries were then coated into the copper current collector using a doctor blade system. The coating speed was set at 0.1 m/min and a range of coating gap sizes were examined, resulting in electrodes with varying thicknesses (11−48 μm) as seen in detail in Table 1. Most electrodes were dried for at least 30 min at 50 °C except electrodes 8, 10, and 11 that were dried at 30 °C. The difference in drying temperature was initially designed as a separate electrode-manufacturing protocol to study the effect. However, no significant difference on electrochemical or cycle life performance between the samples dried at 50 and 30 °C was observed. The copper current collector had a thickness of 9 μm and a diameter of 14.8 mm. Before cell assembly, all of the anodes were subjected to heat treatment at 120 °C under vacuum overnight to remove any humidity residuals. For cell assembly, the graphite electrode had a diameter of 14.8 mm, the lithium metal (Alfa Aesar, 99.9% metal basics) counter

https://doi.org/10.1021/acsaem.3c00488
ACS Appl. Energy Mater. XXXX, XXX, XXX−XXX

Table 1. Electrode Characteristics of All Examined Samples Included in This Study in Ascending Active Mass

sample no.	active mass (mg)	electrode thickness (μm)	density (g/cm^3)	porosity (%)
1	3.03 ± 0.08	14.1 ± 2.1	1.663 ± 0.221	33.0 ± 8.9
2	3.08 ± 0.24	18.3 ± 1.4	1.285 ± 0.006	48.2 ± 0.23
3	3.19 ± 0.21	11.4 ± 0.6	2.121 ± 0.070	14.6 ± 2.8
4	3.52 ± 0.40	22.1 ± 3.0	1.218 ± 0.043	50.9 ± 1.8
5	3.56 ± 0.33	18.1 ± 0.9	1.494 ± 0.071	39.8 ± 2.8
6	3.90 ± 0.6	17.4 ± 0.6	1.706 ± 0.040	31.3 ± 1.6
7	3.97 ± 0.15	23.2 ± 1.0	1.305 ± 0.040	47.4 ± 1.6
8	4.46 ± 0.31	20.6 ± 1.4	1.645 ± 0.053	33.7 ± 2.1
9	4.47 ± 0.29	17.7 ± 0.7	1.917 ± 0.044	22.8 ± 1.8
10	4.83 ± 0.32	22.1 ± 1.3	1.667 ± 0.065	32.8 ± 2.6
11	4.91 ± 0.27	31.7 ± 3.6	1.192 ± 0.151	52.0 ± 6.1
12	5.11 ± 0.22	29.0 ± 1.6	1.344 ± 0.021	45.8 ± 0.8
13	5.54 ± 0.33	32.9 ± 2.5	1.286 ± 0.062	48.2 ± 2.5
14	5.93 ± 0.23	26.0 ± 2.1	1.741 ± 0.079	29.9 ± 3.2
15	6.74 ± 0.10	41.7 ± 0.6	1.229 ± 0.008	50.5 ± 0.3
16	6.92 ± 0.38	26.5 ± 2.3	1.996 ± 0.083	19.6 ± 3.3
17	8.21 ± 0.28	30.0 ± 0.9	2.078 ± 0.020	16.3 ± 0.8
18	9.45 ± 0.28	48.3 ± 0.5	1.487 ± 0.050	40.1 ± 2.0

electrode had a diameter of 15 mm and mass between 7.9 and 20.4 mg, and a GF/A 1820-047 (borosilicate glass fiber) separator manufactured by Whatman with a thickness of 260 μm and pore size of 1.6 μm was cut to a diameter of 16 mm. The electrolyte used was PuriEL Battery Electrolyte (R&D 281) 1.0 M LiPF6 in EC/EMC (ethylene carbonate/ethyl methyl carbonate) = 3/7 (v/v) + 1% wt VC (vinylene carbonate) from Soulbrain (Michigan). 100 μL of the electrolyte was used per cell. The separator and coin cell components were dried at 50 °C under vacuum for several days before use.

In the cases that underwent calendering before the cell assembly, the anodes were calendered at room temperature (25 °C) at 4 mm/s via a twin-roll calendering apparatus (MTI, MSK-HRP-01). The thicknesses were determined by means of a HEIDENHAIN-METRO 2500 system with an accuracy of ±0.2 μm and repeatability of 0.09 μm. For all 18 samples, three individual cells were employed, and their average is provided with the error bars being based on standard deviation. The characteristics of each sample are provided in Table 1. The areal mass loading of active material on the current collectors ranges between 1.76 and 5.49 mg/cm^2. The volume fraction and hence porosity were calculated from the actual electrode densities and the known densities of the electrode components.

2.2. Characterization. *2.2.1. Electrochemical Performance Testing.* A BCS-805 battery cycler (Biologic, France) was used to carry out electrochemical testing. After a resting period of 4 h and open-circuit voltage (OCV) measurement, a formation step was initially performed on all cells in the voltage window 1.5−5 mV, consisting of two discharge−charge cycles, at a constant specific current of 25 mA/g. After the formation step, the cells underwent a direct current internal resistance (DCIR) test for five states of charge (SoC). The DCIR test consisted of two discharge and two charge 5 s pulses separated by a 5 min resting period at a constant specific current of 50 mA/g. To decrease the SoC by 25%, a constant current was applied for 2.5 h at the same specific current followed by a rest period of 1.5 h. A battery capacity determination (BCD) test was performed at a discharge specific current of 100 mA/g. Finally, the cells were cycled 100 times, discharged at 50 mA/g, and charged at 100 mA/g (C/10 and C/5 rates, respectively) in the voltage window of 1.5 V to 5 mV. Three cells were used for each of the 18 electrodes we examined. The voltage−time profile of the protocol is presented in Figure 2 with the DCIR method highlighted for clarity.

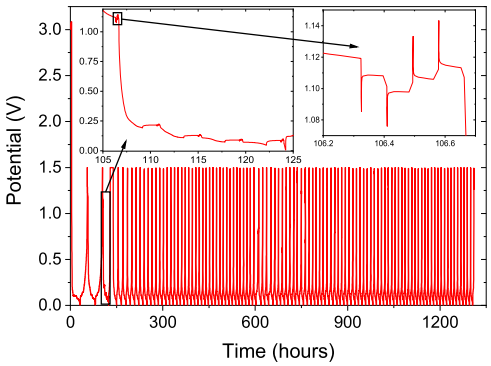

Figure 2. Voltage−time profile with the DCIR method highlighted.

3. RESULTS AND DISCUSSION

The observed DCIR is equivalent to the sum of the series resistance, the charge transfer resistance and the diffusion resistance, or simply the IR drop and forced regime as presented in Figure 1.[38] The discharge and charge resistances are provided separately to compare the difference in lithiation and delithiation due to the reaction kinetics. The discharge and charge resistances are the averages of two pulses each, as it can be observed in Figure 2. Figure 3a shows the DCIR values for three porosities and similar active masses (~3.1 mg). It is clear for all states of charge that the lower porosity values decrease the DCIR. This can be attributed to the reduction in ohmic resistance from the resistance contribution of the electrolyte in the electrode pores and subsequent enhancement of electronic conductivity because of the improved conductive network due to less pores.[36] At low porosities, the lithium-ion diffusion can be hindered due to reduced pore size, increased tortuosity, and hence more difficult lithium-ion diffusion paths and a larger mass transport overpotential.[35] However, in this work due to the short length of the pulse (5 s), we expect to be probing the ohmic resistances and instantaneous reaction kinetics only. The relationship between DCIR and active mass is shown in Figure 3b where it is visible that higher active mass values reduce the DCIR that is indicative of the greater conductive pathways that overall reduce the series resistance.[46] In Figure 3a,b, it is evident that lithiation (black symbols) results in higher values of resistance attributed to intercalation hindrance in the porous electrode and larger charge transfer resistances compared to delithiation (red symbols).[47] Interestingly, this is not the case for 1% SoC were delithiation produces higher resistance values than lithiation. This provides an indication that the remaining Li ions are intercalated at the inner layers of the porous electrode (high pore length) thus impeding delithiation.[48] Furthermore, at 1% SoC, the DCIR values were significantly higher than 25, 50, 75, and 99% SoC, which is due to the low lithium concentration in the active material and hence high reaction overpotential.

After the applied current pulse, a voltage decay curve is observed upon 5 min rest, which relates to the diffusivity of the charged ions. It is likely that the relaxation decay also occurs due to the dispersion of the double layer capacitance at the surface of the particle. At longer times, this is also related to diffusion and any equilibration of lithium ions in the electrolyte and active material. However, due to the short current pulses, negligible levels of lithium are expected to be transported across the surface. These processes occur at different time scales and time constants, and are also characterized by different surface charge. Hence the voltage decay for double

https://doi.org/10.1021/acsaem.3c00488
ACS Appl. Energy Mater. XXXX, XXX, XXX−XXX

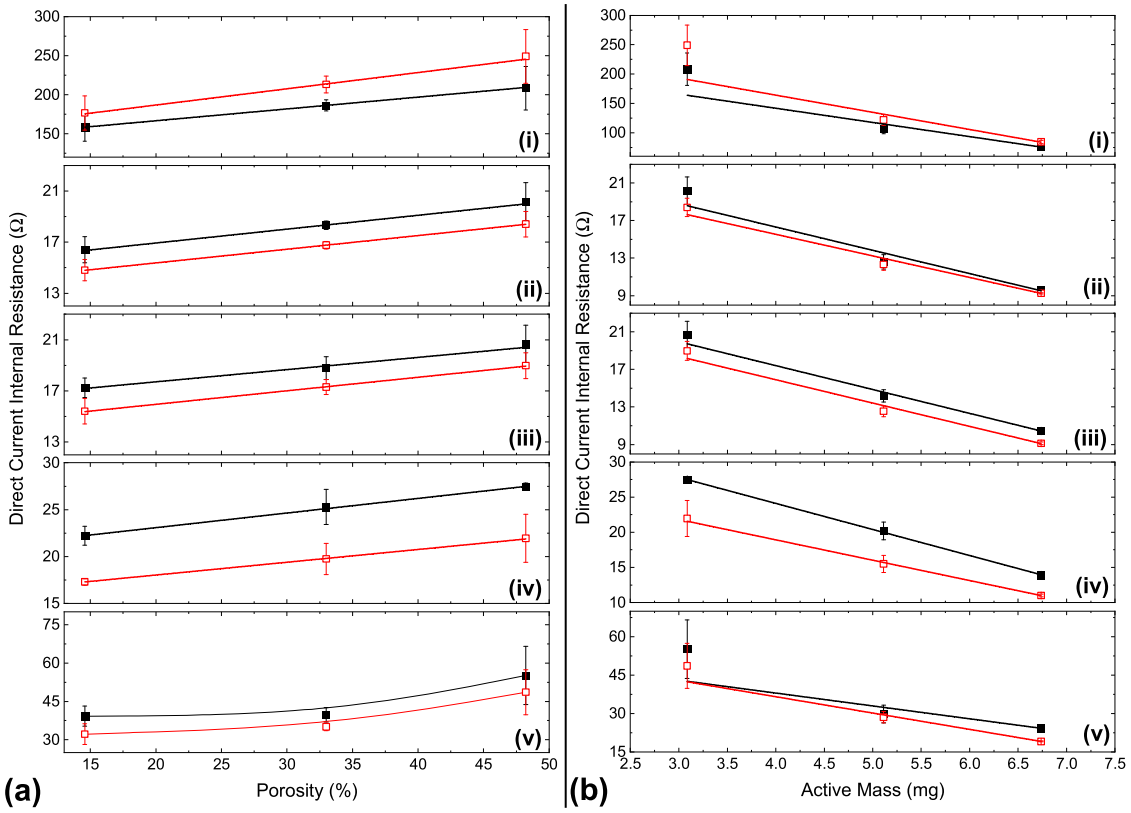

Figure 3. DCIR values obtained at five different states of charge ((i) 1%, (ii) 25, (iii) 50%, (iv) 75%, and (v) 99%) as a function of (a) porosity, for samples with active mass ∼ 3.1 mg, and (b) active mass for samples with porosity ∼ 47%. The black and red symbols correspond to the values obtained during discharge (lithiation) and charge (delithiation).

layer capacitance (DLC) or electric double layer (EDL) is proportional to t^{-1}, whereas the diffusion voltage decay is proportional to $t^{-1/2}$.[49] To account for both contributions, namely, diffusion and electric double layer, the relaxation decay E_{cell} can be modeled as

$$E_{cell}(t) = V_0 - V_{diff} \times [e^{-\sqrt{t/\tau_{diff}}}] - V_{EDL} \times [e^{-(t/\tau_{EDL})}] \quad (1)$$

where V_0 is the plateau voltage with V_{diff} and V_{EDL} being the amplitude voltage values for the diffusion and EDL contributions, respectively. τ_{diff} and τ_{EDL} are the relaxation decay time constants for diffusion and EDL, respectively, with t being the absolute time. In the voltage transient during the current interrupt, the voltage change relating to the EDL and diffusion can be elucidated. An example of the relaxation decay fittings based on eq 1 can be observed in Figure S1. The time constant associated with the surface charge is larger than that of the diffusion, and therefore the initial rate of change of voltage is larger and dominated by the EDL, and at the end of the current interrupt period, the rate of change of voltage is lower and related to diffusion. The fact that relaxation times can be obtained from the DCIR test from the various contributions to relaxation decay indicates that it could be employed as an alternative technique to EIS. Thus, DCIR could save time and resources in an industrial complex and obtain a comparable result. However, it should be noted that EIS is a frequency-dependent technique, and thus direct comparison with DCIR should be done with caution.

The various charge transport and polarization contributions can be discerned by both DCIR and EIS and are described by different time scales or relaxation times, respectively. For example, the voltage transient relating to the surface charge is proportional to $1/t$, whereas the voltage transient relating to diffusion is proportional to $1/\sqrt{(t)}$ as it follows Ficks law of diffusion. Under the framework of linear response theory, the relationship between the time domain and frequency domain is possible through Fourier transformation while the resulting frequency-dependent real and imaginary parts of the complex function obey the Kramers/Kronig relations,[50] which is the mathematical foundation of the Nyquist plot. The results from the voltage relaxation decay fittings during the first lithiation step at the DCIR tests are presented in Figure 4.

In Figure 4a, the effect of state of charge (SoC) upon the IR increase and the diffusion characteristics (voltage amplitude V_{diff} and relaxation decay constant τ_{diff}) are examined. It is evident that with increasing SoC, the voltage amplitude gradually decreases. However, at 99% SoC, the voltage amplitude enhances significantly, indicating the increase of resistance when the graphite/SiO_x electrode is almost completely intercalated. This is supported by the similar trend observed between the IR increase and V_{diff} values against SoC, indicating that at intermediate charge states, diffusion is augmented, while resistance is limited (Ohm's law) with the internal resistance increasing significantly at 99% SoC. The reciprocal trend is observed for the relaxation time of diffusion, thus showing that diffusion occurs faster despite the higher resistance at 99%. It should be noted that the presence of EDL was found significant only at 99% SoC, thus at the rest charge states only, the contribution of diffusion was employed during fittings. The fact that EDL was found insignificant at the rest states of charge could imply that its time scale is much shorter than diffusion, as discussed elsewhere.[39] In other words, in our

https://doi.org/10.1021/acsaem.3c00488
ACS Appl. Energy Mater. XXXX, XXX, XXX−XXX

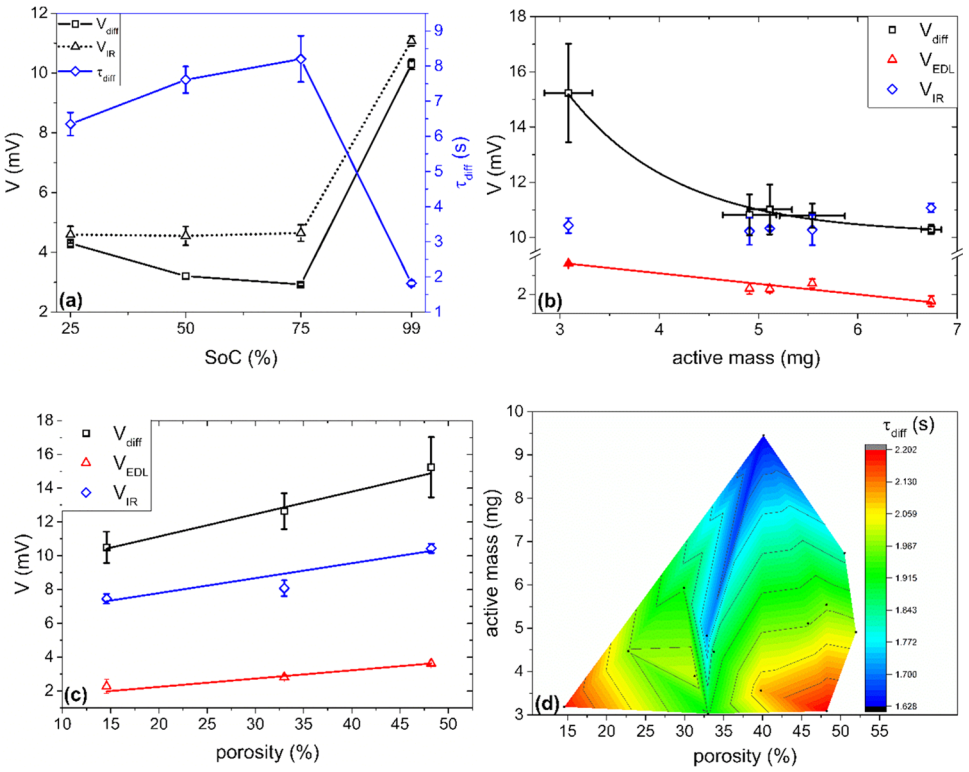

Figure 4. Results obtained from the first lithiation during the DCIR testing. (a) Diffusion characteristics at various states of charge (SoC) for sample 15. (b) Dependence of voltage amplitude against active mass for average porosity values 49 ± 2.4% at 99% SoC for IR increase, diffusion, and EDL. (c) Dependence of voltage amplitude over porosity for average active mass values of 3.1 ± 0.1% mg at 99% SoC for IR increase, diffusion, and EDL. Contour plot representation of the active mass and porosity dependence of the relaxation decay time constant for diffusion at 99% SoC (d). The error bars correspond to standard deviation from the use of three individual cells for each sample and the linear fittings are presented in Table S2.

study, the 5 min relaxation decay is mostly affected by the contribution of diffusion.

As such, the following comparisons between IR increase and the diffusion and EDL fitted voltage amplitudes are solely given at 99% SoC as a function of active mass and porosity in Figure 4b,c, respectively. In either case, the voltage amplitude values for diffusion are significantly higher than EDL, indicating that diffusion is the dominant contribution at the relaxation decay profiles. In Figure 4b, the diffusion and EDL amplitude voltages and the IR increase are provided as a function of active mass for relatively high porosity values (49 ± 2.4%). It is expected that the internal resistance of the electrodes will increase with active mass,[51] which is evident by the gradual enhancement of IR increase values, particularly at the high active mass edge. Since the relaxation decay is recorded after the interruption of the applied current, our findings indicate that at high active masses, the intercalated lithium ions are trapped in the inner layers of the active mass and thus only the ions at the outer layers move. As a result, the diffusion and EDL voltage amplitude values decrease with active mass as depicted in Figure 4b.

In Figure 4c, the diffusion and EDL amplitude voltages and the IR increase are shown against porosity for electrodes at the low active mass regime (3.1 ± 0.1%). A linear trend is observed in both diffusion and EDL cases, suggesting that the pore size is essential for the relaxation of the lithium ions at open-circuit conditions. Between 15 and 35%, the IR increase appears to be constant, while it increases at the high-porosity edge. In comparison to Figure 3a(v), the IR increase exhibits a similar trend with the DCIR with porosity with the latter indicating a sharper increase at the high-porosity edge. This fact indicates that the forced regime enhances at high porosities (greater pore size and hence easier ionic mobility over the short current pulse) that explains the obtained enhancement of the diffusion and EDL voltage amplitudes after the removal of the applied current during the relaxation decay regime. Since diffusion is the dominant contribution, we examine the effect of porosity and active mass at 99% SoC upon diffusion relaxation time, combined at a contour plot presented in Figure 4d. A clear trend is observed with high relaxation time values being observable at the low- and high-porosity edges. Our observations follow the notion that there is an optimum porosity range at which diffusion is facilitated (in agreement with the literature of different graphite-based electrodes[51]), which could be translated as a lower relaxation time (faster process). At low porosities, the pore size is small and thus electrolyte wetting is poor, while at high porosities, the electronic resistance increases significantly.[36] The variations we observe are in the range of 10% (green and red areas at the bottom of the contour plot, Figure 4d). Interestingly, the lowest relaxation time values for diffusion were found for high electrode active masses. As lithium ions are increasingly entrapped in the deeper layers of thicker electrodes, the relaxation decay regime in such high active masses is the result of the mobile ions at the outer layers and hence the lower relaxation times. In any case, over various electrodes, the relaxation times do not differ significantly.

https://doi.org/10.1021/acsaem.3c00488
ACS Appl. Energy Mater. XXXX, XXX, XXX−XXX

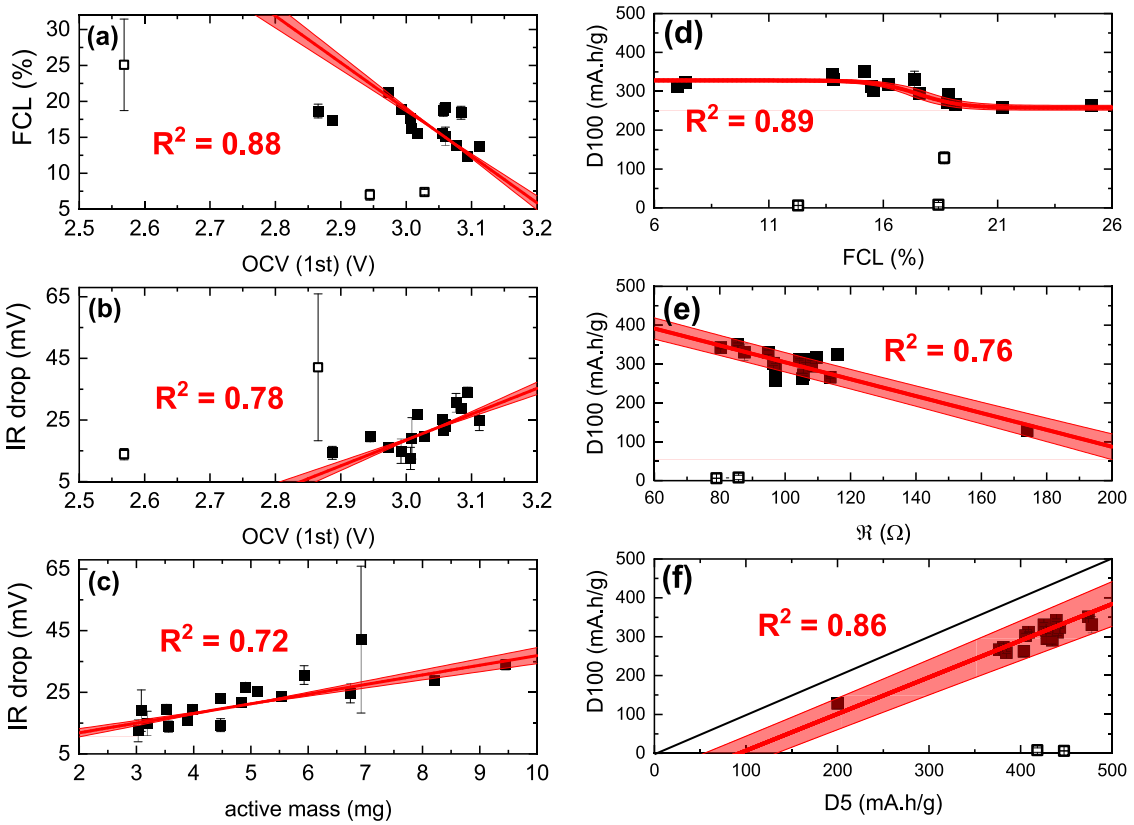

Figure 5. (a) FCL vs the first value of OCV, (b) IR drop obtained just after the formation vs OCV, (c) IR drop vs the active mass, (d–f) discharge specific capacity at the 100th cycle (D100) as a function of (d) FCL, (e) mean of the resistance over cycle life, and (f) discharge specific capacity at the 5th cycle (D5). With closed symbols are the experimental data considered for the fittings and with open symbols are the outliers (as cells that significantly deviated from the general trend that in most cases correspond to the cells with the highest active mass). The R^2 values of the fittings are included in each graph and the parameters of the fitting are provided in Table S1 with all being linear fits apart from panel (d).

Understanding the associations between several physical and electrochemical parameters is an important tool to effectively predict the end electrochemical performance of a battery.[51,52] To achieve this purpose, the first OCV value during the initial rest phase before formation, first cycle loss (FCL), IR drop (measured right after the SEI formation step), and the active mass were combined and presented in Figure 5a–c. The OCV value straight after cell assembly is commonly tested (often by means of a multimeter) as an early indicator of successful cell manufacturing without the requirement of special equipment. Hence, as an early predictor of performance, the first measured value during an open-circuit voltage experiment prior to formation is considered and its relation to FCL and IR drop is shown in Figure 5a,b, respectively. In either case, a linear dependence was found with OCV that is electrode-thickness-dependent, thus indicating that thinner electrodes tend to have higher FCL values but lower IR drops at the present C rate.[53] The electrode thickness effect is also illustrated in Figure S2. The relationship between IR drop and the mass of the electrode is further highlighted in Figure 5c with the values increasing significantly for heavier electrodes.

The discharge specific capacity at the 100th cycle after formation (D100) is given in association with two physical parameters, FCL and the mean of the resistance R, and the discharge specific capacity at an early cycling stage (D5), all presented in Figure 5d–f, respectively. In Figure 5d, D100 has a sigmoidal trend with FCL, highlighting the drop in capacity retention after 100 cycles with increasing irreversible capacity losses obtained during SEI formation. Electrochemical cycle life performance (D100) and "good" SEI formation are strongly correlated; however, there is still significantly more that we need to understand in how to measure or monitor the interface growth.[3,54−56] In order to better understand the mechanism behind the drop in capacity with cycle life, the IR drop values for every 10 cycles were obtained and the corresponding resistance values were calculated with the corresponding discharge currents and presented in Figure S3. It is evident that for most samples, there is a slight increase of resistance with time, being attributed to deterioration from the consecutive lithiation/delithiation cycles that gradually increases the resistance of the SEI layer.[57] To summarize the resistance values over cycle life into one value and thus show the whole resistance history of the cells, we here propose the use of R that is the mean of resistance R over cycle numbers x and is defined according to eq 2 as shown below

$$\mathfrak{R} = \frac{\int (R)\mathrm{d}x}{n} \tag{2}$$

where n is the total number of cycles; in this study, n = 100. A clear decrease of D100 with increasing resistance is visible, indicating that the cells that exhibit the lower average resistances are expected to perform better overall in terms of capacity retention.

A summary of all 18 samples examined in this paper is presented in Figure 5f in a D100 vs D5 representation of the data. A strongly linear trend is observed highlighting that even at the earliest stages of cycling, it is possible to predict the

https://doi.org/10.1021/acsaem.3c00488
ACS Appl. Energy Mater. XXXX, XXX, XXX−XXX

capacity fade later. The correlation between the early stage of cycling (D5) with various cycle numbers (D10, D20, D50, and D100) is presented in Figure S4. Therefore, optimization in an industrial or academic environment can rule out faster cells that do not exhibit the desirable properties and mark them as outliers without investing time, effort, and resources to fully test them. The decay curve for capacity and cycle life is similar for all of these composite electrodes, as the initial high observed specific capacity fades within the first few cycles and reaches equilibrium capacity for the specific capacity of graphite. The contribution to capacity from SiO_x decreases rapidly, likely due to the poor electronic contact after undergoing significant volume expansion. The exact cycle number at which the discharge specific capacity decreases below 372 mAh/g (the theoretical value for graphite) is presented in Table 2. Although the cycle number at which the specific discharge capacity is below 372 mAh/g exhibited no correlation with the physical properties of the electrodes, the plateau value after decay can be connected to initial physical properties as shown later.

Table 2. Electrochemical Characteristics of the Samples Including Their Cycle Life Information as Presented in Figures 5 and S5[a]

sample no.	IR drop (mV)	first cycle loss (%)	D100 (mAh/g)	no. of cycle below 372 mAh/g
1	12.54 ± 3.59	17.58 ± 0.59	294.8 ± 13.9	13
2	19.05 ± 6.73	16.21 ± 0.38	316.8 ± 1.7	13
3	14.86 ± 3.96	18.84 ± 0.56	290.9 ± 10.1	13
4	19.51 ± 1.55	7.00 ± 0.75	312.0 ± 8.7	17
5	13.92 ± 1.82	25.08 ± 6.37	262.4 ± 14.0	8
6	15.96 ± 0.29	21.20 ± 0.09	259.0 ± 1.9	7
7	19.56 ± 0.77	7.38 ± 0.38	323.9 ± 1.9	19
8	22.88 ± 0.47	19.16 ± 0.33	266.4 ± 2.5	6
9	14.34 ± 2.09	17.36 ± 0.66	330.6 ± 21.1	21
10	21.65 ± 0.46	18.78 ± 0.85	272.5 ± 3.5	6
11	26.73 ± 1.34	15.49 ± 0.43	311.8 ± 1.6	10
12	25.21 ± 1.29	15.59 ± 0.54	302.7 ± 6.2	9
13	23.55 ± 0.96	15.15 ± 1.27	351.2 ± 3.1	28
14	30.57 ± 3.03	13.81 ± 0.22	330.6 ± 5.5	13
15	24.75 ± 3.18	13.76 ± 0.20	342.4 ± 3.3	15
16	42.12 ± 23.84	18.66 ± 0.96	128.6 ± 15.2	NA
17	28.86 ± 0.79	18.41 ± 0.90	failed at cycle 70	11
18	33.97 ± 1.65	12.28 ± 0.07	failed at cycle 65	25

[a]Sample 16 was below the theoretical specific capacity of graphite (372 mAh/g) throughout the whole cycle life.

In all cases, the plateau behavior was observed prior to the 50th cycle; hence, for representation purposes, the discharge specific capacity over the cycle life (D_X) was normalized with that of D50 and shown in Figure 6. The normalized discharge capacity was found to vary significantly from sample to sample at the first 30 cycles. In order to investigate this variation between samples, we introduce a new model based on the initially measured physical properties of the electrodes. The empirical model is based on simplicity to serve as a "rule of thumb" in an industrial environment to produce estimations rather than extremely accurate physical predictions. Our goal is to provide a good estimation based on the least physical parameters that can be determined as early as possible, i.e., right after the formation step. An empirical model is proposed in Figure 7 to describe the discharge specific capacity as a function of cycle life based on resistance and porosity shown in eqs 3 later. This effectively shows that the decay in capacity contribution from SiO_x is related to the porosity and resistance and can be easily modeled.

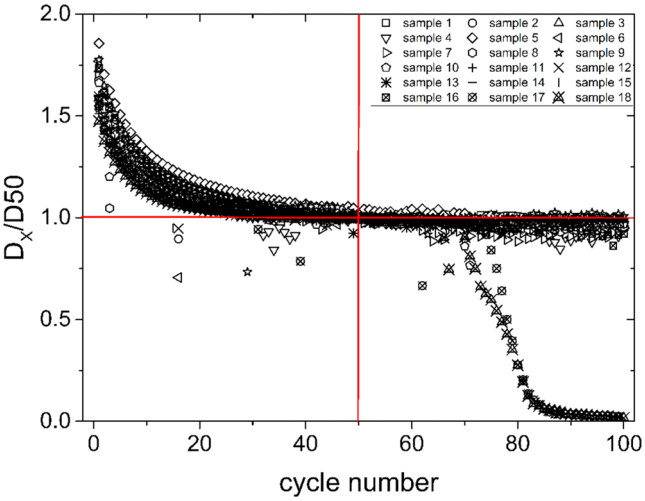

Figure 6. Normalized values of discharged specific capacity over cycle life with the value at the 50th cycle.

The empirical model proposed here to describe the cycle life response is defined according to eqs 3 where D_X and x are the discharge specific capacity over cycle life and the cycle number, respectively, as introduced below

$$D_X = \alpha_1 \mathrm{D5} \times (1 - e^{-\alpha_2 x})^{-\alpha_3} \tag{3a}$$

with a_1, a_2, and a_3 being empirical parameters calculated as

$$\alpha_1 = \frac{\mathrm{D5}}{\mathrm{D50}} = \begin{cases} 0.7647 \pm 0.0161 \ (\pm 2\%) & \text{for porosities over 45\%} \\ 0.7128 \pm 0.0359 \ (\pm 5\%) & \text{for porosities under 45\%} \end{cases} \tag{3b}$$

$$\alpha_2 = (V_{\mathrm{IR}}) \times (P) \times (\mathrm{OCV}) \tag{3c}$$

$$\alpha_3 = \frac{\rho^3 \times P^2}{\mathrm{OCV}} \tag{3d}$$

where D5 and D50 are the values of experimentally measured discharge specific capacities (mA·h/g) at the 5th and 50th cycles after formation, respectively. It was observed that D5/D50 strongly related to porosity, with two distinctive groups being found above and below 45% porosity values, and hence the two different empirical constants. However, the α_1 parameter could be defined in more detail given a larger dataset. V_{IR} corresponds to the IR drop (V) as obtained at the first cycle after formation, P is the porosity fraction (i.e., 50% is 0.5), OCV (V) corresponds to the first value measured during an open-circuit voltage experiment before formation, and ρ is the density (g/cm^3) of the electrode. Porosity fraction and density are interconnected but for simplicity reasons they both appear in the proposed empirical model, with the relation connecting the two been presented in eqs 4 later. Extremely good fits to the capacity fade are observed with this equation

https://doi.org/10.1021/acsaem.3c00488
ACS Appl. Energy Mater. XXXX, XXX, XXX−XXX

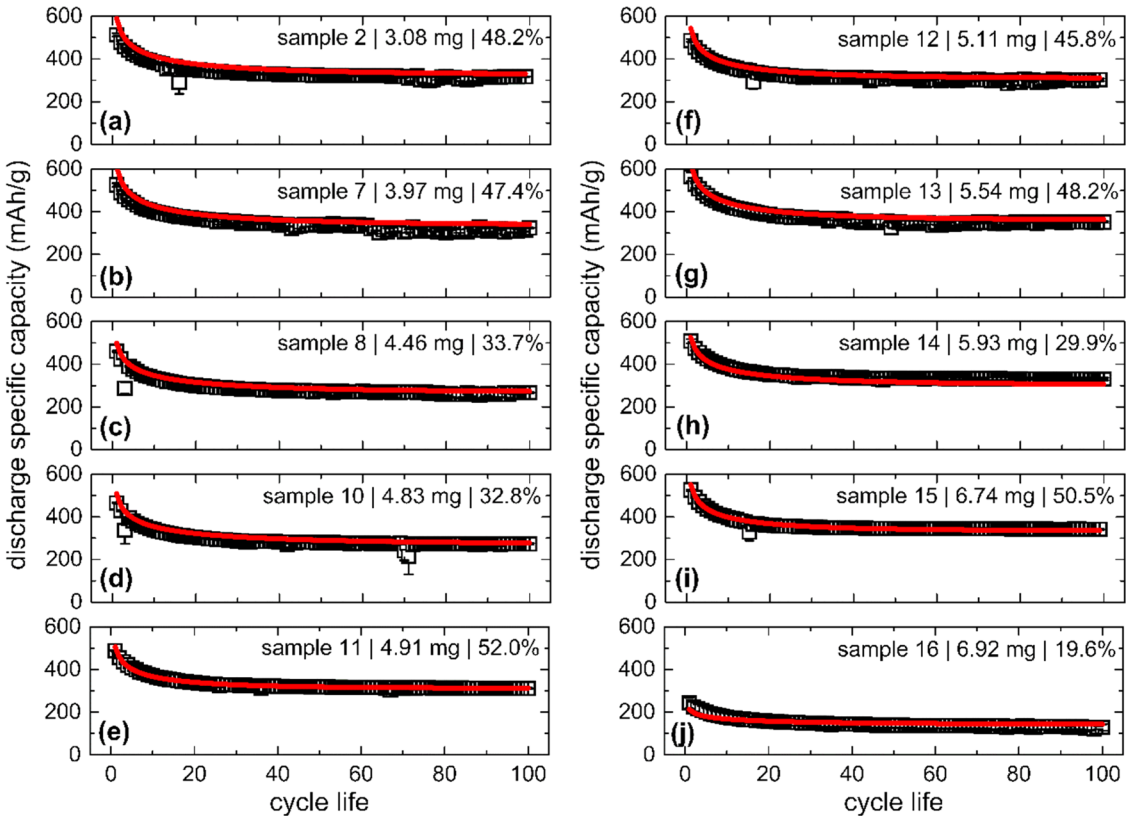

Figure 7. Discharge specific capacity as a function of cycle number of 10 samples, namely, samples (a) 2, (b) 7, (c) 8, (d) 10, (e) 11, (f) 12, (g) 13, (h) 14, (i) 15, and (j) 16. The solid symbols correspond to the experimental values (averages of three individual cells) and the red fitting lines follow eqs 3 first introduced here. Complete information about the cells is given in Table 1. The fittings of the remaining samples are provided in Figure S5.

(Figure 7) and may give us an alternative route to predicting capacity vs cycle life for mixed composite electrodes. It is interesting to highlight that this model described the cycle life down to the plateau value but not during cell degradation as shown by samples 17 and 18 (Figures 6 and S5). In order to describe the degradation of the cells, a larger dataset is required, and the empirical model of eqs 3 could be built further and predict the full discharge specific capacity.

Porosity fraction (P) relates to density (ρ) via eqs 4 seen below

$$P = 1 - \rho \sum_n \left(\frac{w_n}{\rho_n} \right) \tag{4a}$$

$$\rho = \frac{m_e}{l_e A_e} \tag{4b}$$

where n is the number of solid constituent materials used during mixing with w_n and ρ_n being the weight fraction and density of each individual constituent, respectively. m_e, l_e, and A_e are the electrode's mass, thickness, and active area as determined experimentally during cell making.

In Figure 8, the two key parameters of eqs 3, IR drop and porosity fraction, are isolated to examine how they individually affect the model. It should be noted that here, according to eqs 4, all information of density variation is considered within the porosity fraction variation. It is evident that both physical properties affect the rate at which discharge capacity fades at the initial stage of cycle life. The inset within Figure 8a shows that the model accurately describes the dependence of discharge capacity upon IR drop.[51,53] IR drop is a measure of the internal resistance of the electrode and hence is reversely associated with the discharge capacity. On the other hand, the effect that porosity has is more complicated, as shown in Figure 8b inset. Two peaks are observed at 30 and 50%, respectively. However, the second peak could be artificial since a higher α_1D5 constant for porosities over 45% is employed, as discussed previously in eqs 3. It is generally accepted that a fine-tuned porosity value is required to achieve the optimum discharge capacity, a porosity value that depends on the characteristics of the electrode.[36] According to the proposed model, this fine-tuned porosity value is in the vicinity of 30%, which is close to experimentally observed values for graphite-based electrodes.[51]

4. CONCLUSIONS

In the present study, graphite-SiO_x composite electrodes were developed and tested with carrageenan gum as a water-soluble binder. In total, 54 individual cells were developed, divided into 18 cases. The cases were categorized by active mass in the range of 3−10 mg and various porosities between 15 and 50%. The electrochemical characterization was categorized in three sections: the formation step, a current pulse and relaxation test (DCIR) at various states of charge, and the cycle life. The fast DCIR characterization employed here gives a simpler alternative to EIS to obtain information of the contributing factors, ion diffusion, and EDL from the relaxation decay. In the examined time scales, the contribution of the active mass and porosity to the ohmic resistance is notable. The porosity of

https://doi.org/10.1021/acsaem.3c00488
ACS Appl. Energy Mater. XXXX, XXX, XXX−XXX

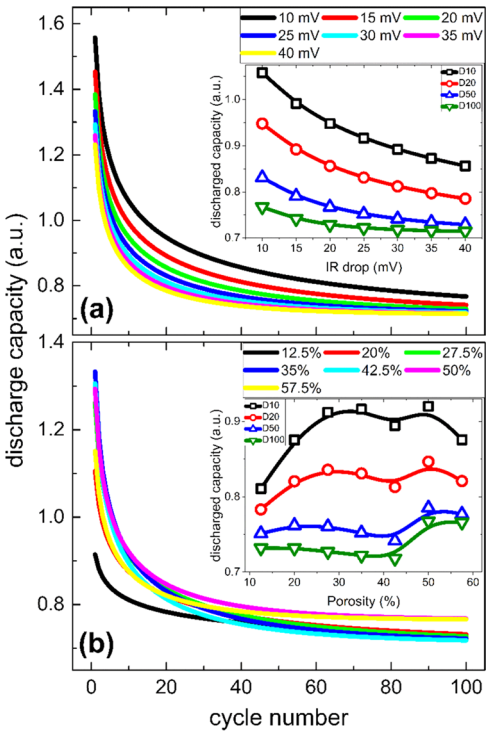

Figure 8. Examination of the key parameters (IR drop and porosity) of the proposed model presented in eqs 3, with α_1D5 being equal to 0.7647 or 0.7128 for porosities over or under 45%, respectively, and OCV = 3. (a) IR drop variation for P fraction = 0.35 and (b) porosity fraction variation for IR drop = 0.025 V. As insets, the dependences of IR drop and porosity upon D10, D20, D50, and D100 are shown.

the electrode is important for obtaining better electrical contact over time, as shown via the DCIR test; however, improvements in the flexibility of the active material with binders and conductive additives is required.

During the cycle life of the developed cells, it became evident that the capacity contribution of SiO_x degrades rapidly over the first 20−30 cycles. The decay in cycle life can be fitted using an empirical model proposed here (eqs 3), thus relating the porosity and resistance of the electrode to the discharge specific capacity over cycle life. The overall electrochemical behavior of the investigated cells showed that the decrease in the capacity contribution from SiO_x is due to the decrease in the connectivity of SiO_x with the electronic additives, causing likely isolation of SiO_x particles and thus not participation in the active mass. This effect results in a gradual internal resistance increase over cycle life and indicates a connection with porosity. The empirical model fitted to the capacity decay with cycle life indicates that porosity and electronic conductivity are key parameters. This method can lead to early indication of cycle life failures, resulting in faster electrode optimization. Future work to investigate this further will be with other mixed material and single material electrodes with different binder systems.

■ ASSOCIATED CONTENT

Data Availability Statement

Further information and requests for resources and materials should be directed and will be fulfilled by the Lead Contact, E.K. The data will be available through Mendeley data (DOI: 10.17632/vmczyckhmk.2).

Supporting Information

The Supporting Information is available free of charge at https://pubs.acs.org/doi/10.1021/acsaem.3c00488.

Fitting parameters used to describe the functions employed in Figures 3, 4, and 5 (Tables S1, S2, and S3); relaxation decay fitting showing both the diffusion and EDL contributions to the voltage profile (Figure S1); effect that electrode thickness has upon first cycle loss (FCL), open-circuit voltage (OCV) prior to formation, and IR drop after formation (Figure S2); resistance values calculated by eq 2 as a function of cycle number for each sample (Figure S3); discharge specific capacity as a function of the discharge specific capacity at the 5th cycle (D5) is provided at various cycles (Figure S4); and effect of cycle life upon the values of the discharge specific capacity for samples 1, 3−6, 9, 17, and 18, including the fitting based on eqs 3 (Figure S5) (PDF)

■ AUTHOR INFORMATION

Corresponding Author

Emma Kendrick − *The Energy Materials Group, School of Metallurgy and Materials, University of Birmingham, Birmingham B15 2TT, United Kingdom; The Faraday Institution, Didcot OX11 0RA, United Kingdom;* orcid.org/0000-0002-4219-964X; Phone: +44(0) 1214146730; Email: E.Kendrick@bham.ac.uk

Authors

Stavros X. Drakopoulos − *The Energy Materials Group, School of Metallurgy and Materials, University of Birmingham, Birmingham B15 2TT, United Kingdom; The Faraday Institution, Didcot OX11 0RA, United Kingdom;* orcid.org/0000-0002-6798-0790

Thomas Cowell − *The Energy Materials Group, School of Metallurgy and Materials, University of Birmingham, Birmingham B15 2TT, United Kingdom*

Complete contact information is available at: https://pubs.acs.org/10.1021/acsaem.3c00488

Author Contributions

Conceptualization, visualization, writing—original draft, and writing—review and editing: S.X.D., E.K.; data curation and formal analysis: S.X.D.; funding acquisition, project administration, resources, and supervision: E.K.; investigation: S.X.D., T.C.; methodology: S.X.D., T.C., E.K.

Notes

The authors declare no competing financial interest.

■ ACKNOWLEDGMENTS

This work was supported by the Faraday Institution NEXTRODE project (faraday.ac.uk; EP/S003053/1, FIRG015). The authors thank Dr. Carl D. Reynolds (University of Birmingham) for assisting in slurry mixing and Dr. Yongxiu Chen (University of Birmingham) for fruitful discussions about direct current internal resistance measurements.

■ REFERENCES

(1) Goodenough, J. B.; Park, K.-S. The Li-Ion Rechargeable Battery: A Perspective. *J. Am. Chem. Soc.* **2013**, *135*, 1167−1176.

(2) Yoshino, A. The Birth of the Lithium-Ion Battery. *Angew. Chem., Int. Ed.* **2012**, *51*, 5798−5800.
(3) Lopez, I. R.; Lain, M. J.; Kendrick, E. Optimisation of Formation and Conditioning Protocols for Lithium-Ion Electric Vehicle Batteries. *Batteries Supercaps* **2020**, *3*, 900−909.
(4) Lakhdar, Y.; Geary, H.; Houck, M.; Gastol, D.; Groombridge, A. S.; Slater, P. R.; Kendrick, E. Optimization of Electrode and Cell Design for Ultrafast-Charging Lithium-Ion Batteries Based on Molybdenum Niobium Oxide Anodes. *ACS Appl. Energy Mater.* **2022**, *5*, 11229−11240.
(5) Jabbour, L.; Bongiovanni, R.; Chaussy, D.; Gerbaldi, C.; Beneventi, D. Cellulose-Based Li-Ion Batteries: A Review. *Cellulose* **2013**, *20*, 1523−1545.
(6) Chun, S.-J.; Choi, E.-S.; Lee, E.-H.; Kim, J. H.; Lee, S.-Y.; Lee, S.-Y. Eco-Friendly Cellulose Nanofiber Paper-Derived Separator Membranes Featuring Tunable Nanoporous Network Channels for Lithium-Ion Batteries. *J. Mater. Chem.* **2012**, *22*, 16618.
(7) Lee, B.; Ko, Y.; Kwon, G.; Lee, S.; Ku, K.; Kim, J.; Kang, K. Exploiting Biological Systems: Toward Eco-Friendly and High-Efficiency Rechargeable Batteries. *Joule* **2018**, *2*, 61−75.
(8) Harper, G.; Sommerville, R.; Kendrick, E.; Driscoll, L.; Slater, P.; Stolkin, R.; Walton, A.; Christensen, P.; Heidrich, O.; Lambert, S.; Abbott, A.; Ryder, K.; Gaines, L.; Anderson, P. Recycling Lithium-Ion Batteries from Electric Vehicles. *Nature* **2019**, *575*, 75−86.
(9) Gastol, D.; Marshall, J.; Cooper, E.; Mitchell, C.; Burnett, D.; Song, T.; Sommerville, R.; Middleton, B.; Crozier, M.; Smith, R.; Haig, S.; McElroy, C. R.; van Dijk, N.; Croft, P.; Goodship, V.; Kendrick, E. Reclaimed and Up-Cycled Cathodes for Lithium-Ion Batteries. *Global Challenges* **2022**, *6*, No. 2200046.
(10) Winter, M.; Besenhard, J. O.; Spahr, M. E.; Novák, P. Insertion Electrode Materials for Rechargeable Lithium Batteries. *Adv. Mater.* **1998**, *10*, 725−763.
(11) Yazami, R.; Touzain, Ph. A Reversible Graphite-Lithium Negative Electrode for Electrochemical Generators. *J. Power Sources* **1983**, *9*, 365−371.
(12) Liu, J.; Wang, S.; Sun, Q. All-Carbon-Based Porous Topological Semimetal for Li-Ion Battery Anode Material. *Proc. Natl. Acad. Sci. U.S.A.* **2017**, *114*, 651−656.
(13) de las Casas, C.; Li, W. A Review of Application of Carbon Nanotubes for Lithium Ion Battery Anode Material. *J. Power Sources* **2012**, *208*, 74−85.
(14) Guerfi, A.; Charest, P.; Dontigny, M.; Trottier, J.; Lagacé, M.; Hovington, P.; Vijh, A.; Zaghib, K. SiO −Graphite as Negative for High Energy Li-Ion Batteries. *J. Power Sources* **2011**, *196*, 5667−5673.
(15) Chung, S.-Y.; Bloking, J. T.; Chiang, Y.-M. Electronically Conductive Phospho-Olivines as Lithium Storage Electrodes. *Nat. Mater.* **2002**, *1*, 123−128.
(16) Flandrois, S.; Simon, B. Carbon Materials for Lithium-Ion Rechargeable Batteries. *Carbon* **1999**, *37*, 165−180.
(17) Rezqita, A.; Hamid, R.; Schwarz, S.; Kronberger, H.; Trifonova, A. Conductive Additive for Si/Mesoporous Carbon Anode for Li-Ion Batteries: Commercial Graphite vs Carbon Black C65. *ECS Trans.* **2015**, *66*, 17−27.
(18) Guy, D.; Lestriez, B.; Bouchet, R.; Gaudefroy, V.; Guyomard, D. Tailoring the Binder of Composite Electrode for Battery Performance Optimization. *Electrochem. Solid-State Lett.* **2005**, *8*, A17.
(19) Wang, Y.; Dang, D.; Li, D.; Hu, J.; Cheng, Y.-T. Influence of Polymeric Binders on Mechanical Properties and Microstructure Evolution of Silicon Composite Electrodes during Electrochemical Cycling. *J. Power Sources* **2019**, *425*, 170−178.
(20) Reynolds, C. D.; Slater, P. R.; Hare, S. D.; Simmons, M. J. H.; Kendrick, E. A Review of Metrology in Lithium-Ion Electrode Coating Processes. *Mater. Des.* **2021**, *209*, No. 109971.
(21) Nirmale, T. C.; Kale, B. B.; Varma, A. J. A Review on Cellulose and Lignin Based Binders and Electrodes: Small Steps towards a Sustainable Lithium Ion Battery. *Int. J. Biol. Macromol.* **2017**, *103*, 1032−1043.
(22) Wang, C.; Ma, Y.; Du, X.; Zhang, H.; Xu, G.; Cui, G. A Polysulfide Radical Anions Scavenging Binder Achieves Long-life Lithium−Sulfur Batteries. *Battery Energy* **2022**, *1*, No. 20220010.
(23) Reynolds, C. D.; Lam, J.; Yang, L.; Kendrick, E. Extensional Rheology of Battery Electrode Slurries with Water-Based Binders. *Mater. Des.* **2022**, *222*, No. 111104.
(24) Jiang, M.; Mu, P.; Zhang, H.; Dong, T.; Tang, B.; Qiu, H.; Chen, Z.; Cui, G. An Endotenon Sheath-Inspired Double-Network Binder Enables Superior Cycling Performance of Silicon Electrodes. *Nano−Micro Lett.* **2022**, *14*, 87.
(25) Mobarak, N. N.; Jumaah, F. N.; Ghani, M. A.; Abdullah, M. P.; Ahmad, A. Carboxymethyl Carrageenan Based Biopolymer Electrolytes. *Electrochim. Acta* **2015**, *175*, 224−231.
(26) Chen, H.; Ling, M.; Hencz, L.; Ling, H. Y.; Li, G.; Lin, Z.; Liu, G.; Zhang, S. Exploring Chemical, Mechanical, and Electrical Functionalities of Binders for Advanced Energy-Storage Devices. *Chem. Rev.* **2018**, *118*, 8936−8982.
(27) Mu, P.; Zhang, H.; Jiang, H.; Dong, T.; Zhang, S.; Wang, C.; Li, J.; Ma, Y.; Dong, S.; Cui, G. Bioinspired Antiaging Binder Additive Addressing the Challenge of Chemical Degradation of Electrolyte at Cathode/Electrolyte Interphase. *J. Am. Chem. Soc.* **2021**, *143*, 18041−18051.
(28) Ma, Y.; Wang, C.; Ma, J.; Xu, G.; Chen, Z.; Du, X.; Zhang, S.; Zhou, X.; Cui, G.; Chen, L. Interfacial Chemistry of γ-Glutamic Acid Derived Block Polymer Binder Directing the Interfacial Compatibility of High Voltage LiNi0.5Mn1.5O4 Electrode. *Sci. China Chem.* **2021**, *64*, 92−100.
(29) Li, Z.; Wan, Z.; Wu, G.; Wu, Z.; Zeng, X.; Gan, L.; Liu, J.; Wu, S.; Lin, Z.; Gao, X.; Ling, M.; Liang, C. A Biopolymer Network for Lean Binder in Silicon Nanoparticle Anodes for Lithium-Ion Batteries. *Sustainable Mater. Technol.* **2021**, *30*, No. e00333.
(30) Kazda, T.; Capková, D.; Jaššo, K.; Straková, A. F.; Shembel, E.; Markevich, A.; Sedlaříková, M. Carrageenan as an Ecological Alternative of Polyvinylidene Difluoride Binder for Li-S Batteries. *Materials* **2021**, *14*, 5578.
(31) Jang, W.; K K, R.; Thorat, G. M.; Kim, S.; Kang, Y.; Kim, T.-H. Lambda Carrageenan as a Water-Soluble Binder for Silicon Anodes in Lithium-Ion Batteries. *ACS Sustainable Chem. Eng.* **2022**, *10*, 12620−12629.
(32) Forouzan, M. M.; Chao, C.-W.; Bustamante, D.; Mazzeo, B. A.; Wheeler, D. R. Experiment and Simulation of the Fabrication Process of Lithium-Ion Battery Cathodes for Determining Microstructure and Mechanical Properties. *J. Power Sources* **2016**, *312*, 172−183.
(33) Kendrick, E. Advancements in Manufacturing. In *Future Lithium-ion Batteries*; Eftekhari, A., Ed.; Royal Society of Chemistry: Cambridge, 2019; Chapter 11, pp 262−289.
(34) Meyer, C.; Bockholt, H.; Haselrieder, W.; Kwade, A. Characterization of the Calendering Process for Compaction of Electrodes for Lithium-Ion Batteries. *J. Mater. Process. Technol.* **2017**, *249*, 172−178.
(35) Sheng, Y.; Fell, C. R.; Son, Y. K.; Metz, B. M.; Jiang, J.; Church, B. C. Effect of Calendering on Electrode Wettability in Lithium-Ion Batteries. *Front. Energy Res.* **2014**, *2*, No. 56.
(36) Shim, J.; Striebel, K. A. Effect of Electrode Density on Cycle Performance and Irreversible Capacity Loss for Natural Graphite Anode in Lithium-Ion Batteries. *J. Power Sources* **2003**, *119−121*, 934−937.
(37) Schweiger, H.-G.; Obeidi, O.; Komesker, O.; Raschke, A.; Schiemann, M.; Zehner, C.; Gehnen, M.; Keller, M.; Birke, P. Comparison of Several Methods for Determining the Internal Resistance of Lithium Ion Cells. *Sensors* **2010**, *10*, 5604−5625.
(38) Kim, J. H.; Lee, S. J.; Lee, J. M.; Cho, B. H. In *A New Direct Current Internal Resistance and State of Charge Relationship for the Li-Ion Battery Pulse Power Estimation*, IEEE 7th Internatonal Conference on Power Electronics, Daegu, South Korea, 2007; pp 1173−1178.
(39) Lacey, M. J.; Edström, K.; Brandell, D. Visualising the Problems with Balancing Lithium−Sulfur Batteries by "Mapping" Internal Resistance. *Chem. Commun.* **2015**, *51*, 16502−16505.

https://doi.org/10.1021/acsaem.3c00488
ACS Appl. Energy Mater. XXXX, XXX, XXX−XXX

(40) Lacey, M. J. Influence of the Electrolyte on the Internal Resistance of Lithium−Sulfur Batteries Studied with an Intermittent Current Interruption Method. *ChemElectroChem* **2017**, *4*, 1997−2004.
(41) Chien, Y.-C.; Liu, H.; Menon, A. S.; Brant, W. R.; Brandell, D.; Lacey, M. J. A Fast Alternative to the Galvanostatic Intermittent Titration Technique. *Nature Communications* **2023**, DOI: 10.1038/s41467-023-37989-6.
(42) Ratnakumar, B. V.; Smart, M. C.; Whitcanack, L. D.; Ewell, R. C. The Impedance Characteristics of Mars Exploration Rover Li-Ion Batteries. *J. Power Sources* **2006**, *159*, 1428−1439.
(43) Kurisawa, I.; Iwata, M. In *Internal Resistance and Deterioration of VRLA Battery-Analysis of Internal Resistance Obtained by Direct Current Measurement and Its Application to VRLA Battery Monitoring Technique*, IEEE Proceedings of Power and Energy Systems in Converging Markets, Melbourne, VIC, Australia, 1997; pp 687−694.
(44) Chien, Y.-C.; Menon, A. S.; Brant, W. R.; Brandell, D.; Lacey, M. J. Simultaneous Monitoring of Crystalline Active Materials and Resistance Evolution in Lithium−Sulfur Batteries. *J. Am. Chem. Soc.* **2020**, *142*, 1449−1456.
(45) Theuerkauf, D.; Swan, L. Characteristics of Open Circuit Voltage Relaxation in Lithium-Ion Batteries for the Purpose of State of Charge and State of Health Analysis. *Batteries* **2022**, *8*, 77.
(46) Gallagher, K. G.; Nelson, P. A.; Dees, D. W. Simplified Calculation of the Area Specific Impedance for Battery Design. *J. Power Sources* **2011**, *196*, 2289−2297.
(47) Garrick, T. R.; Kanneganti, K.; Huang, X.; Weidner, J. W. Modeling Volume Change Due to Intercalation into Porous Electrodes. *J. Electrochem. Soc.* **2014**, *161*, E3297−E3301.
(48) Ogihara, N.; Itou, Y.; Sasaki, T.; Takeuchi, Y. Impedance Spectroscopy Characterization of Porous Electrodes under Different Electrode Thickness Using a Symmetric Cell for High-Performance Lithium-Ion Batteries. *J. Phys. Chem. C* **2015**, *119*, 4612−4619.
(49) Wu, J. Understanding the Electric Double-Layer Structure, Capacitance, and Charging Dynamics. *Chem. Rev.* **2022**, *122*, 10821−10859.
(50) *Broadband Dielectric Spectroscopy*; Kremer, F.; Schönhals, A., Eds.; Springer: Berlin, 2003.
(51) Drakopoulos, S. X.; Gholamipour-Shirazi, A.; MacDonald, P.; Parini, R. C.; Reynolds, C. D.; Burnett, D. L.; Pye, B.; O'Regan, K. B.; Wang, G.; Whitehead, T. M.; Conduit, G. J.; Cazacu, A.; Kendrick, E. Formulation and Manufacturing Optimization of Lithium-Ion Graphite-Based Electrodes via Machine Learning. *Cell Rep. Phys. Sci.* **2021**, *2*, No. 100683.
(52) Niri, M. F.; Reynolds, C.; Román Ramírez, L. A.; Kendrick, E.; Marco, J. Systematic Analysis of the Impact of Slurry Coating on Manufacture of Li-Ion Battery Electrodes via Explainable Machine Learning. *Energy Storage Mater.* **2022**, *51*, 223−238.
(53) Abe, Y.; Hori, N.; Kumagai, S. Electrochemical Impedance Spectroscopy on the Performance Degradation of LiFePO4/Graphite Lithium-Ion Battery Due to Charge-Discharge Cycling under Different C-Rates. *Energies* **2019**, *12*, 4507.
(54) Yoon, T.; Chapman, N.; Seo, D. M.; Lucht, B. L. Lithium Salt Effects on Silicon Electrode Performance and Solid Electrolyte Interphase (SEI) Structure, Role of Solution Structure on SEI Formation. *J. Electrochem. Soc.* **2017**, *164*, A2082−A2088.
(55) Pathan, T. S.; Rashid, M.; Walker, M.; Widanage, W. D.; Kendrick, E. Active Formation of Li-Ion Batteries and Its Effect on Cycle Life. *J. Phys. Energy* **2019**, *1*, No. 044003.
(56) Kishore, B.; Chen, L.; Dancer, C. E. J.; Kendrick, E. Electrochemical Formation Protocols for Maximising the Life-Time of a Sodium Ion Battery. *Chem. Commun.* **2020**, *56*, 12925−12928.
(57) Mandli, A. R.; Kaushik, A.; Patil, R. S.; Naha, A.; Hariharan, K. S.; Kolake, S. M.; Han, S.; Choi, W. Analysis of the Effect of Resistance Increase on the Capacity Fade of Lithium Ion Batteries. *Int. J. Energy Res.* **2019**, *43*, 2044−2056.

https://doi.org/10.1021/acsaem.3c00488
ACS Appl. Energy Mater. XXXX, XXX, XXX−XXX